JAAS

Development of X-ray imaging of intracellular elements and structure

Journal:	*Journal of Analytical Atomic Spectrometry*
Manuscript ID	JA-CRV-03-2020-000128.R1
Article Type:	Critical Review
Date Submitted by the Author:	15-May-2020
Complete List of Authors:	Matsuyama, Satoshi; Osaka University, Department of Precision Science and Technology, Graduate School of Engineering; SPring-8 Center Maeshima, Kazuhiro; NIG, Genome Dynamics Laboratory, Research Organization of Information and Systems; SPring-8 Center; SOKENDAI, Department of Genetics Shimura, Mari; NCGM, Dept. of Intractable Diseases; SPring-8 Center

Review

Development of X-ray imaging of intracellular elements and structure

Satoshi Matsuyama[ab], Kazuhiro Maeshima[bcd]

and Mari Shimura[be#]

[a]Department of Precision Science and Technology, Graduate School of Engineering, Osaka University, Suita, Osaka 565-0871, Japan

[b]RIKEN SPring-8 Center, 1-1-1 Kouto, Sayo, Hyogo 679-5148, Japan

[c]Genome Dynamics Laboratory, National Institute of Genetics, Research Organization of Information and Systems, Mishima, Shizuoka 411-8540, Japan

[d]Department of Genetics, SOKENDAI, Mishima, Shizuoka 411-8540, Japan

[e]Department of Intractable Diseases, Research institute, National Center for Global Health and Medicine, Tokyo 162-8655, Japan

Abstract (199/250)

The desire to see the smallest possible objects, such as the contents of cells, reflects our intellectual curiosity and has resulted in the development of various types of microscopes. Microscopes using an X-ray source were developed after Röntgen's discovery of X-rays in 1895. Röntgen rays were first used for photography in 1896 and for observation of the structural details of biological samples in the 1900s. This use of X-rays grew considerably following the development of X-ray optics such as diffractive lenses and total-reflection mirrors in the late 1940s. X-ray microscopy theoretically has better resolution than that of visible light (400–700 nm) microscopy and has developed differently from both visible light and electron microscopy due to the penetration ability of X-rays. The third-

generation synchrotron radiation facilities that produce higher electron beam energies promoted X-ray microprobes for various types of microscopies. The accompanying development of X-ray focusing systems has led to today's submicron X-ray probes, which have high enough resolution for imaging cells at the organelle level. In this review, we describe the imaging technologies using synchrotron X-ray fluorescence by means of a sub-100-nm focusing system and X-ray diffraction, which facilitates the determination of the cellular elemental distribution and structure.

1. Introduction

Imaging cells using X-rays: From the Röntgen era to the present. Observations of cells using X-rays began soon after Röntgen's discovery of X-rays in 1895. Goby initiated the observation of biological samples using X-ray microscopy and named it "microradiography"[1]. This X-ray microscopy was developed with mirror optics for improved resolution[2, 3], and evolved earlier than the development of electron microscopy. The resolving power of X-ray microscopy was intermediate between that of electron microscopy and light microscopy, and the penetration ability of the X-rays was highest among them. This characteristic resulted in X-ray microscopy developing differently from visible light and electron microscopies. Transmission X-ray microscopy (TXM) or scanning X-ray transmission microscopy (STXM) were established in the 1970s at the University of Göttingen[4-6]. STXM became available for imaging cellular structures, such as nuclei, nucleoli, membranes, and chromosomes by amplitude contrast (Fig. 1). Various modifications were then applied. For brighter and higher-resolution biological imaging,

soft X-ray sources with incoherent illumination were developed[7]. To detect specific cellular proteins, TXM was coupled with antibody peroxidase-conjugated antibody and silver staining[8]. To excite visible light emissions, scanning luminescence X-ray microscopy (SLXM) was also developed[7], which can capture images of selected structures in cells using dyes or secondary antibodies coupled with lanthanide polychelates[9]. Another outgrowth of X-ray microscopy occurred after the development of the third-generation synchrotron radiation facilities, which produced higher electron beam energies[10-14]. The Advanced Photon Source (APS) at Argonne National Laboratory equipped a beamline covering the 0.5–4 keV (soft X-ray) and 4–30 keV (hard X-ray) range with an STXM. The European Synchrotron Radiation Facility (ESRF) in Grenoble, France, developed X-ray fluorescence microscopy (XRF) with an X-ray focusing system, a zone plate, that detected elements in human cartilage samples[15]. SPring-8 in Japan equipped a beamline up to 100 keV[16, 17]. The hard X-rays at these third-generation synchrotron radiation facilities produced microprobes and the X-rays were further focused with focusing systems, such as Kirkpatrick-Baez (KB) mirrors and a zone plate (Fig. 2), that provide sufficiently high resolution for observing cells, even at the organelle level. Notably, synchrotron X-ray microscopy became a powerful tool for visualizing cellular structures and contents such as elements, elemental valences and oxidation states, and structures (Fig. 3).

2. Current cell imaging systems using synchrotron X-rays

2.1. Development of an X-ray focusing system. To develop X-ray microscopy for single-cell imaging, an intense focused beam with a sub-100-nm width is essential. However, prior to the development of our first scanning X-ray fluorescence microscopy (SXFM) around 2005, no X-ray focusing optics systems were available that satisfied the requirements for spectromicroscopy, namely, high throughput, sharp focus, and achromaticity. Therefore, we developed a high-performance X-ray focusing system with ultraprecise total-reflection elliptical mirrors. Our focusing optics system is based on two total-reflection mirrors arranged perpendicular to each other (KB mirrors[18]; Fig. 4). Due to the total-reflection phenomenon, the system has the advantages of good throughput and no chromatic aberrations. However, construction of the mirror is challenging and there are often residual fabrication errors and surface roughness, which degrade spatial resolution and reflectivity. The tolerances for fabrication errors and surface roughness are ~4 nm (peak-to-valley) and ~0.5 nm (root mean square [rms]), respectively. Achieving both the perfect shape and good surface roughness using conventional mirror fabrication methods is challenging. This was overcome by our super-polishing technique, called elastic emission machining (EEM)[19]. EEM can perform very precise shaping together with atomic-scale smoothing. Using EEM, a fabrication error of ~2 nm and surface roughness of ~0.2 nm rms on the mirrors can be obtained (Fig. 4). To determine the achievable minimum focus size and reflectivity, focusing tests were performed at a synchrotron radiation facility (BL29XUL of SPring-8). The obtained focus size was 48 nm (V) × 36 nm (H) [20] and the reflectivity of double reflection was ~60% (Fig. 4). The focus size approximately reached the diffraction limit (48 nm (V) × nm 29 (H)). In addition, reflectivity was in good agreement with the ideal value. These results suggest that mirrors were successfully fabricated with the required accuracy. Other systems with

different focusing systems are also available for observing intracellular elements[21]; however, each system has its own advantages and disadvantages.

2.2 SXFM system. Imaging of multiple elements in tissues and cells is now feasible. Laser ablation inductively coupled plasma-mass spectrometry (LA-ICP-MS), microparticle-induced X-ray emission (microPIXE), and XRF are established methods[22-28]. MicroPIXE has the advantage of being fully quantitative in combination with backscattering spectrometry[29]; however, further improvements in detection limits and resolution are expected through the use of XRF with synchrotron microprobes. In this review, we introduce an SXFM system that uses our originally developed X-ray focusing system. SXFM was developed specifically for imaging single cells (Fig. 5). To image elements at the single-cell level, we developed a prototype XRF consisting of KB mirrors, a detector (silicon drift detector, SDD), and scanning stages. An SDD in combination with a fast multichannel analyzer can record all X-ray spectra of each pixel within the measurement area. Recording all spectra of each pixel enables selection of elements for the production of elemental maps after an experiment and also enables processing of the obtained spectra using peak-separation and noise reduction algorithms. The scanning stage requires high resolution for measurement and a long travel range to identify regions of interest (ROIs). Therefore, a stepping-motor-driven XZ stage was used that had a high-precision linear encoder with a minimum step of 1 nm and a travel range of 25 mm. Fig. 6 shows high-resolution elemental mapping of a test pattern[30]. We successfully visualized elemental distributions with 30–50 nm resolution.

2.3. User-friendly upgrades to SXFM. Although we developed SXFM for single-cell imaging, the system was not sufficiently polished for use by biological scientists. For practical applications, especially in biology and medicine, a user-friendly system is desirable. To this end, we added a sample changer, an optical differential interference contrast (DIC) microscope (reflection type; numerical aperture = 0.25, magnification ×10), and graphical user interface-based software (Fig. 7a). The sample changer consists of a motorized θ stage and can hold 12 samples, which can be observed for prolonged periods without interruption. This contributes to greater stability of observation because the ambient temperature is disturbed by sample introduction. The software controls the sample changer and the DIC microscope, as well as the X-ray focusing system, detector system, and scanning stage. The area of interest can be measured by drawing a rectangle on the DIC image in the software. In this way, only the cells of interest are selected and observed. The developed SXFM system has a zoom function enabled by a size-variable focused beam, which is controlled by a slit downstream of the light source used as a vertical source; the beam width is controllable from the diffraction limit (~40 nm) to 1,000 nm with little change in flux density (Fig. 7b). This enables both observations with a large field-of-view and a short acquisition time using a large beam and observations with high resolution using a small beam. This facilitates the identification and observation of cells of interest. To identify cells, an area of 400 μm × 400 μm is scanned, within which a single cell and an ROI within that cell are observed. From the results, the detection limit (3σ) was estimated to be ~10^{-2} fg for elements heavier than Fe and 0.1–1 fg for lighter elements[31, 32]. This difference is due to various factors, such as the absorption coefficient and fluorescence yield.

2.4 Application in cell biology

2.4.1 Sample preparation. Obtaining images of cells in their natural state to the greatest possible degree is a major issue in various imaging fields[33]. Trials on living cells using different radiation absorbed doses (10^4-10^5 Gy) were performed in the 1990s[34]. Although it was anticipated that electron microscopy was likely applicable to living cells, the morphology of cells and their function in terms of cellular uptakes were significantly disturbed by soft X-rays[35]. Notably, exposure to only 3 Gy caused alteration of cellular growth and colony formation[36]. Then, wet cell samples with chemical fixation were examined. Cells fixed with formaldehyde (2%) were relatively resistant to radiation damage, although significant cellular ultrastructural change was a concern[35, 37, 38](Fig. 8). The radiation damage by X-ray microscopy precluded the observation of cells with normal physiological functions. While Kirz et al. have discussed this in depth since 1995[35], it is still a subject of concern.

As synchrotron X-rays also damage cells due to the production of free radicals, living cells cannot be visualized by SXFM. Even wet cell samples with chemical fixation compromise the measurements. To prepare samples for SXFM, cells are often fixed with 2% paraformaldehyde and dried after washing with buffer (Fig. 9). Using this method, we have not observed severe radiation damage such as that seen in wet samples in the 1990s. However, this preparation alters the natural distribution of elements[39]. Surprisingly, most free ions, such as K and Ca, disappear after fixation with paraformaldehyde and washing with phosphate-buffered saline (PBS), whereas half of the Fe remains. In contrast, Zn and Cu levels are relatively unchanged (Fig. 10). Therefore, it may be that only elements bound to cellular molecules remain after fixation. We recently recommended flash freezing for SXFM (see Section 2.4.2, “Cryo-SXFM”).

Flash freezing is used to maintain a natural state for other microscopy techniques, such as electron microscopy and LA-ICP-MS[40, 41]. Flash freezing also suppresses free radical production resulting from irradiation. We also proposed freeze-drying after flash freezing (Fig. 9), which has the advantages of long-term storage of valuable samples, easy transportation, and measurement at room temperature. On the other hand, fixed-dried samples can also provide valuable information with appropriate controls if the obtained data are repeatable.

Recently, X-ray free-electron lasers (XFELs) with femtosecond pulse duration enabled single-shot diffraction imaging of a living cell without radiation damage (see Section 3.3.1 "Solving the limitations of both spatial resolution and radiation damage")[42]. Diffraction data could be obtained within 7 fs, before Coulomb explosion—in other words, prior to the start of cell damage by XFELs—whereas cells were extremely damaged after Coulomb explosion and the sample measurement was no longer repeatable. X-ray fluorescence imaging is not suitable for XFELs at present; however, future technology such as the development of single-shot imaging by full-field X-ray fluorescence microscopy (FXFM)[43] may resolve this issue. We hope that XFELs can advance our understanding of living cells.

2.4.2 Cryo-SXFM. Because SXFM requires several hours to visualize trace elements and intense X-rays damage cells, live cells cannot be used. As an alternative, frozen-hydrated cells prepared by rapid freezing can be used by biologists and medical scientists. This method is frequently employed for cryo-electron microscopy, which has been used for 30 years. In this method, cells are rapidly frozen at a rate of $> 10^5$ K/s, so that vitreous ice forms rather than large ice crystals that destroy the ultrastructure of cells, thus preserving

the cell morphology[44]. In what ways does cryo-SXFM differ from cryo-electron microscopy? Cryo-SXFM was developed by overcoming several engineering problems, such as issues with KB mirror optics caused by temperature changes and vibrations from the refrigerator[39] (Fig. 11, top). Our cryo-SXFM is equipped with a compact, vibration-free refrigerator that cools by means of Joule-Thomson expansion of a high-pressure gas. The temperature of the frozen cells is maintained at 126 K. In addition, both the elemental distributions and morphology of cells must be preserved during sample preparation, unlike in cryoelectron microscopy. To satisfy this requirement, we developed a sample preparation method specialized for SXFM applications[39]. This method involves rinsing cultured cells with specially prepared buffer containing none of the elements of interest for elemental mapping of frozen-hydrated cells. The buffer contains 261 mM glucose and 9 mM acetic acid in 10 mM Tris buffer to maintain osmotic pressure of 280 mOsm and pH of 7.4. This results in removal of the excess salts that alter the detection of elements with high sensitivity. Next, samples are rapidly frozen using liquid ethane or propane. The thickness of the extra ice layer is reduced by sublimation under vacuum by slowly and slightly warming the sample. This is done to reduce elastic and inelastic scattering, which degrade sensitivity. Fig. 11 (bottom) shows the elemental distributions. The K, Ca, and Fe distributions are different from those in chemically fixed cells[39]. In contrast, the Zn and Cu distributions are similar to those of chemically fixed cells. Investigation of the elemental contents of cells by ICP-MS yielded results similar to the SXFM mapping data (Fig. 10). Thus, a rapid freezing method should be employed for visualizing elemental distributions, particularly those of ionic elements[45].

2.4.3 Quantification of XRF signals using cellular samples. The adherent cells on the basement can be easily observed, as seen in Fig. 1; however, it is difficult to estimate actual concentration units where irradiated. The thickness of the cells is usually the maximum at the center of nucleus and decreases toward the periphery. Additionally, cells are not always smooth. Since the actual thickness of cells (volume) is difficult to measure, signal intensity per area ($\mu g/cm^2$) is often used for XRF. We made a calibration curve for semiquantitative analysis using fluorescence signals from platinum films, in which the element levels were determined in advance. A color scale was added to show the semiquantitatively determined levels of elements in the irradiated area (see Section 2.4.4.2). We must keep in mind that the signals obtained were superimposed from the top to the bottom of the cells where irradiated. Relatively ubiquitously distributed elements such as zinc could be helpful for understanding the signals or distributions of other elements. On the other hand, sections of tissues or cells seem easier to use for estimating the thickness (volume); however, such sections are not always precisely flat on the basement.

2.4.4 Challenges to understanding the metabolome at the single-cell level. Imaging of proteins has been well-studied using immunofluorescence microscopy; however, cells have other molecules such as fatty acids and sugars, as well as metals/elements. These molecules and chemical species seem to function mutually and give rise to functional variation. Thus, the concept of the metabolome (metallome) has developed. Imaging of these molecules as well as proteins will no doubt contribute to understanding precise and well-organized cellular functions.

2.4.4.1 High-resolution images for intracellular elements using thin cross-sectioning. We prepared 500-nm cryo-sections of cells by the Tokuyasu method[46, 47] (Fig. 9) to obtain better spatial resolution because X-rays superimpose the three-dimensional (3D) distribution of elements in the cells on two-dimensional (2D) images. Sectioning thinner than 500 nm is not practical for SXFM imaging due to the limited availability of synchrotron beam time; however, this will be possible in the near future due to faster scans (see Section 3, "Future Plans"). It is notable that higher signal intensities of P formed islands at the nucleus, suggesting a high concentration of nucleic acids (Fig. 12). Spot-like distributions of Fe were likely located in these P islands. On the other hand, Zn was separate from the Fe and P. The data suggested that each element binds to a different molecule at a different location for the functions of nuclei. Thin sectioning is available at present; however, tomography or CT imaging would be useful for high spatial resolution to understand cellular functions in the near future.

2.4.4.2 Imaging intracellular fatty acids. A single-element-labeled fatty acid combined with SXFM enabled observation of metabolites in cells such as phospholipids and neutral lipids (Fig. 13a). Fatty acids had been difficult to visualize because of problems with labeling molecules larger than fatty acids. Indeed, chromophore labeling was often used; however, labeling with lager molecules may interfere with fatty acids metabolism by steric hindrance. On the other hand, radioisotope labeling with an imaging system and DESI-MS or label-free MALDI-MS imaging is not presently adequate for the observation of intracellular lipids. Single-element (Br)-labeled fatty acids are metabolized in cells, resulting in many different saturated or unsaturated fatty acids (mostly phospholipids and

neutral lipids), which was confirmed by LC-MS[48]. Additionally, our SXFM visualized Br as a spot-like distribution in the cytoplasm using X-ray of 250 nm/pixel (Fig. 13b). Combined images from different microscopes with SXFM images were effective for characterizing these signals. We obtained DIC, phase contrast, and fluorescence images before acquiring SXFM images (Figs. 14a and b). A laser-fabricated cell basement for SXFM with a grid is useful for merging of images obtained by different microscopy techniques (Fig. 14c). The grid indicated the slightest changes in size between different samples preparations. Images from SXFM were merged with conventional direct fluorescence staining of the ER/Golgi, where various enzymes that metabolize fatty acids are present, and suggested co-localization with the distribution of Br spots (Figs. 14a and b). Single-element labeling combined with SXFM technology is expected to be useful for imaging other metabolites in cells. Labeling of different elements would allow us to see multi-colored images for different kinds of cellular molecules.

2.5 Coherent X-ray diffraction imaging

We next introduce another way to visualize intracellular organelle structures. Imaging with hard X-rays is an indispensable tool for the nondestructive and quantitative visualization of the internal structures of thick specimens in medicine, materials science, and biology. In conventional hard X-ray imaging, image contrast results from variations in X-ray absorption arising from density differences and variations in the composition and thickness of the object. However, the detection sensitivity is low, particularly for materials consisting of light elements, such as soft biological materials, because of low X-ray absorption. Phase contrast in X-ray imaging was first reported in 1995[49, 50] and has high sensitivity beyond absorption contrast as previously stated. X-ray phase-contrast

imaging has attracted interest for potential medical applications. However, the spatial resolution of hard X-ray imaging techniques for weakly scattering objects is still poor and limited by X-ray focusing optics. Coherent X-ray diffraction imaging (CXDI)[51] is X-ray imaging without a lens and has spatial resolution better than that of conventional X-ray microscopy. This procedure is advantageous for investigating the detailed structures of large objects such as cellular organelles chromosomes, or nuclei for which crystals cannot be obtained.

When a non-crystallized object is illuminated by coherent, monochromatic hard X-rays with known phase, a continuous diffraction pattern called 'speckles' is obtained (Fig. 15b). In light microscopy, this kind of diffraction from an object is converted into real image by lenses, but good optical lenses for hard X-rays are not available. Almost 20 years ago it became possible to convert the speckle diffraction pattern into a real image by computational calculations instead of using lenses[52]. If the speckle diffraction pattern is recorded finely enough to satisfy the oversampling condition, which is derived from the Shannon sampling theorem[53], the structure can be reconstructed by using an iterative phase retrieval method, a computational process for finding a structure to fit the diffraction pattern[54]. We can say that CXDI is a 'lensless' high-resolution X-ray microscopy method.

Using CXDI, we observed a human chromosome without staining[55]. Chromosomes are essential cellular organelles for the transmission of copied long DNA into two daughter cells during cell division[56]. Moreover, chromosomes are a suitable target for X-ray diffraction and microscopy because DNA, which is the main component of the chromosome, is rich in P and produces high contrast. Indeed, although the mechanism by

which long strands of DNA are globally organized into the chromosomes is unclear[56], small-angle X-ray diffraction has shown the rather irregular nature of local chromosome structure[57-59]. A schematic view of CXDI of a human chromosome at SPring-8 is shown in Fig. 15a. The coherent diffraction (speckles) from the chromosome was recorded with an X-ray direct-detection charge-coupled device. From the speckles (Fig. 15b), an image of the chromosome was reconstructed. A 2D reconstruction of the chromosome is shown in grayscale (Fig. 16a) and color scale (Fig. 16b) on a scale where the intensities are proportional to the projection of the electron density. The spatial resolution of the 2D reconstruction is 38 nm. For 3D reconstruction, we obtained data at different incident angles ranging from –70° to +70° (38 diffraction datasets). A reconstructed 3D electron-density map of the chromosome is shown in Fig. 16c. We estimated the spatial resolution of the 3D reconstruction to be 120 nm. This was the first 3D electron-density mapping of an unstained cellular organelle using CXDI[55].

3. Future plans

3.1 Combination with other microscopy techniques. XRF is suitable for detecting essential elements, such as Fe, Ni, Cu, Zn, and others up to Br, before scattering X-ray peaks, but the detection of low-atomic-number elements such as C, O, and N is problematic due to their low absorption and the dominance of Auger electron emission over X-ray fluorescence emission in the excitation process. Combinations of images from low-atomic-number elements such as H, C, O, N, and Na by soft X-ray microscopy or nanoscale secondary ion mass spectrometry (NanoSIMS)[60] with elemental mapping

images would be a challenge worth tackling. Another promising approach would be to combine XRF images with structural images such as CXDI[61].

3.2 Upgrading the X-ray focusing system. The sensitivity and spatial resolution of SXFM will be enhanced by improving the light source and focusing optics. At present, undulator X-ray light sources at SR facilities are commonly used because of their brightness and small source size. However, the source size is not small enough to focus X-rays down to a few tens of nanometers with a limited demagnification factor. Therefore, we had to install a slit or pinhole to produce a virtual small source. However, this resulted in loss of a large quantity of X-ray photons at the slit. Thus, the focus size and beam intensity have a trade-off relationship. This is a common problem in spectroscopy using focused X-ray beams. Fortunately, construction of so-called ultimate (or diffraction-limited) storage ring light sources as next-generation X-ray sources is underway globally[62], including MAX IV in Sweden, Sirius in Brazil, ESRF-Upgrade in France, APS-Upgrade in the United States, and SPring-8 II in Japan. For example, SPring-8 II, which is an upgrade of SPring-8 to an ultimate storage ring, can provide a very small source of 24.0 μm (H) × 5.6 μm (V) (rms) without using a virtual source. Such a small source will enable the production of an intense nanobeam with a photon flux of ~10^{14} photons/s and focus size of 230 nm (H) × 120 nm (V) (full width at half-maximum [FWHM])[63]. This intensity is ~1,000-fold that of the nanobeam used in our SXFM. This intense nanobeam will facilitate 1,000-fold faster scans or $\sqrt{1000}$ (≈ 30)-fold increase in sensitivity for the same exposure time. Additionally, the current focusing optics can be improved to have higher resolution. The promising focusing optics method for this purpose is multilayer KB mirrors utilizing Bragg reflection (Fig. 17a). Such mirrors can

reflect X-rays with a 2–3-fold higher grazing-incidence angle than total-reflection mirrors, which leads to a large numerical aperture and small diffraction limit. A focus size of 7 nm was achieved using Pt/C multilayer mirrors at SPring-8 in combination with a deformable mirror as a phase compensator[64, 65] (Fig. 17a). Further improvements are expected in reflectivity, fabrication accuracy of the mirror substrate, cost, and manufacturing period. In the near future, multilayer KB mirrors that can provide a sub-10-nm focused beam will become available for practical applications.

In addition, a versatile system is desirable. The optical parameters of focusing systems, such as focal length and incident angle, are fixed. Therefore, the sample position cannot be changed even if the sample is larger than usual or a heater or cooler is required temporarily. Also, the grazing-incident angle cannot be changed according to the X-ray energy to accept input X-rays effectively. Versatility may be achieved by the introduction of deformable mirrors, which can realize adaptive X-ray focusing. Ultraprecise deformable mirrors for nanofocusing have been developed (Fig. 17b). Recently, diffraction-limited focusing to a focus size of 65 nm was achieved using piezoelectric bimorph mirrors, which can produce arbitrary deformation of the mirror shape by applying a voltage to the attached piezoelectric elements[66]. These techniques are expected to be used for practical experiments in the near future, which would enable detection of smaller targets with better resolution in biology and medicine.

3.3 Future X-ray diffraction images.

3.3.1 Solving the limitations of both spatial resolution and radiation damage. Since the spatial resolution of microscopy is determined by the wavelength used, hard X-rays can, in principle, achieve atomic resolution. With hard X-rays generated at third-

generation synchrotron radiation facilities, spatial resolution is often limited by radiation damage or by the intensity of the X-rays. Both of these limitations can be removed or lessened dramatically by the use of XFELs to produce high peak-brilliance coherent hard X-rays with ultrafast (~fs) pulses: High-resolution images can be obtained before radiation damage occurs by using XFEL with sub-10-fs pulse duration. In fact, Kimura et al. succeeded in taking a snapshot image of a live bacterial cell at the nanometer level by using an X-ray focusing system as described above at the XFEL facility SACLA[42, 67, 68] (Fig. 18a).

3.3.2 Solving the limitation of sample size. As originally conceived, CXDI has a plane-wave geometry, in which the sample is illuminated with an X-ray plane wave. Up to now, plane-wave CXDI has been used to observe weakly scattering objects of biological specimens. However, plane-wave CXDI has a significant limitation: the sample must be an isolated object of less than a few micrometers in size. Scanning CXDI, which is called X-ray ptychography, was a breakthrough that overcame this limitation. A probe is scanned across the sample and the diffraction pattern is observed at each beam position. Recently, high-resolution ptychography using focused X-ray beams and 2D and 3D imaging for biological applications have been reported by Takahashi et al[69]. (Fig. 18b).

Conclusion

X-rays have been a useful technology enabling various types of microscopy**.** Going forward, imaging of multiple intracellular elements at the single-cell level or the structures of organelles using synchrotron X-rays will be further developed by advanced technologies. These technologies will enhance our understanding of various cellular functions and may reveal unknown mechanisms.

Acknowledgments

We thank Takashi Kimura at Hokkaido University for providing gridded basements, Yasumasa Joti at Riken, Yukio Takahashi at Tohoku University, and Yoshinori Nishino at Hokkaido University for critical reading of this manuscript and Tetsuya Ishikawa at Riken for advice and encouragement during the development of SXFM. We also acknowledge Akihiro Matsunaga at NCGM for measurements and analyses of images, Yoshiki Kohmura at Riken for assistance with the beamline adjustment and helpful discussion. This study was supported by CREST of the Japan Science and Technology Agency (MS, SM); MS was supported by a Grant-in-Aid for Research on Advanced Medical Technology from MHLW, the NCGM Intramural Research Fund (29A1020), and Grant-in-Aid for Challenging Exploratory Research by MEXT (17K19417). KM was supported by JSPS (16H04746 and 19H05273), the Takeda Science Foundation, and a JST CREST (JPMJCR15G2).

Figure legends

Fig 1. Scanning X-ray transmission micrograph (STXM) of fibroblasts by Gilbert in the 1990s[35]. Reproduced with permission of the copyright owner.

Fig 2. Representative X-ray focusing systems.

Fig 3. Many ways to use synchrotron X-rays.

Fig 4. Schematic of Kirkpatrick-Baez (KB) mirror optics together with the residual error in the elliptical shape and characterized intensity profile at the focus in the vertical direction.

Fig 5. Schematic of the scanning X-ray fluorescence microscopy (SXFM) system.

Fig 6. High-resolution W and Ga maps of a test pattern. Left, Ga test pattern prepared by focused ion beam (FIB). Right, SXFM images of the W and Ga test pattern. Exposure = 1 s/pixel, scanning step = 15 nm/pixel, and X-ray energy = 15 keV. The figure was reproduced from Matsuyama et al., Rev. Sci. Instrum. 2006 with permission of the copyright owner[30].

Fig 7. SXFM became user friendly. **(a)**, Photograph of the user-friendly SXFM (left) and graphical user interface-based software (right). **(b)**, Zoom function of the SXFM. The sample was HeLa cells. X-ray energy = 15 keV.

Fig 8. Radiation damage to wet chromosomes reported by Williams in the 1990s[38]. V. *faba* chromosomes were fixed with 0.2% glutaraldehyde and imaged by scanning transmission X-ray microscopy (STXM) in physiological buffer. Multiple images of the same chromosome showed degradation due to radiation damage (lower); however, the initial images (First images) showed mass and diameter measurements similar to those of the previously unexposed ones (0-10^0 Gy, Multiple images). Reproduced with permission of the copyright owner.

Fig 9. Diagram showing sample preparation protocols for SXFM. The inset photo shows a sample holder that can set three samples on a motorized θ stage for SXFM (see Section 2.3 User-friendly upgrades to SXFM).

Fig 10. Leakage of intracellular elements due to fixation. Average elemental contents (K, Ca, Fe, Cu, and Zn) of cells measured by inductively coupled plasma-mass spectrometry (ICP-MS). Sample preparation is described below. A, Cells were cultured for 2 days and then 10^7 cells were collected by centrifugation. B, Cells were washed with PBS and fixed with 4% paraformaldehyde in PBS for 10 min. C, Cells were permeabilized for 5 min with 0.2% Triton X-100 (Sigma-Aldrich, St. Louis, MO) in PBS, washed with PBS. The K, Ca, Fe, Cu, and Zn contents of samples A, B, and C were measured by ICP-MS. The axis in the chart shows the ratios of B and C to A. The figure was reproduced from Matsuyama et al., X-ray Spectrom., X-ray Spectrom. 2010 with permission of the copyright owner[39].

Fig 11. Schematic and photograph of cryo-scanning x-ray fluorescence microscopy (SXFM) (top), and elemental distribution maps of frozen-hydrated cells (bottom). The figure was reproduced from Matsuyama et al., X-ray Spectrom. 2010 with permission of the copyright owner[39].

Fig 12. Images of intracellular P, Zn, and Fe mapping in multiple myeloma cells. Photographs of cryo-sections (500 nm thick) of cells were obtained using the following parameters: exposure = 1 s/pixel, scanning step = 250 nm/pixel, X-ray energy = 15 keV. Bar, 10 μm. The white border indicates the nuclear region. The figure was reproduced from Shimura and Matsuyama, JSR 2010 with permission of the copyright owner.

Fig 13. SXFM images of Br-labeled fatty acid. **(a)** Zn-, and Br-mapping images of Br-labeled stearic acids (Br-SA) and EtOH-treated CHO-K1 cells. Cells were treated with Br-SA for 24 h. Br and Zn mapping images taken with 600 nm/pixel X-ray beam size. Arrows indicate the Br signals, which tended to be clustered. **(b)** Higher-resolution X-ray fluorescence images of Br-labeled palmitic acid (Br-PA). Left, Br and Zn mapping images taken with an X-ray beam size of 250 nm/pixel. Cells were treated with Br-PA for 24 h. Right, a surface plot generated based on the red area in the left images. Red arrows, the direction presented in the surface plots; white arrows, the spot-like Br distribution. Br, BrKα X-ray emission line. A brighter color indicates higher signal intensity. Color bar, fg/μm^2; bar, 10 μm. The figures were modified from Shimura, FASEB J 2016 with permission of the copyright owner[48].

Fig 14. Merged images from different microscopies. **(a)** Comparison between a marker of endoplasmic reticulum, DiOC6(3) fluorescence image and Br signals from SXFM (500 nm/pixel). **(b) T**he area framed in yellow in (**a)** was observed using higher-resolution SXFM (250 nm/pixel). DIC, differential interference contrast images; DiOC6(3), fluorescence dye signals; Br-PA, SXFM signals from BrKα; phase-contrast, phase-contrast images. Merged image, red, DiOC6(3); green, Br; bar, 10 μm; bar in Br, fg/μm^2. **(c)** DIC images of a 200-nm-thick gridded SiN basement. Cells were plated on the basement, fixed with paraformaldehyde and dried overnight at room temperature. DIC, differential interference contrast microscopy; Bar, 20 μm. The figures were modified from Shimura, FASEB J 2016[48].

Fig 15. X-ray diffraction microscopy (XDM) for observation of chromosomes in cells. **(a)** Schematic view of XDM measurement of an unstained human chromosome at BL29XUL in SPring-8. **(b)** The coherent diffraction (speckles) from the chromosome. The panels were reproduced from Nishino et al., 2009[55] with permission of the copyright owner.

Fig 16. A two-dimensional reconstruction of a human chromosome is shown in grayscale, **(a)** and color, **(b)**. Note that the intensities are proportional to the projection of the electron density. An arrow indicates the centromere region. **(c)**, Reconstructed 3D electron-density map of the chromosome. Cross-sectional images of the chromosome at 409-nm intervals are shown. The panels were reproduced from Nishino et al., 2009[55] with permission of the copyright owner.

Fig 17. Future SXFM technologies. **(a)** X-ray focusing using multilayer KB mirrors. (i) Schematic and (ii) obtained beam profile at the focus. The figure was reproduced from Yamauchi et al., J. Phys. Condens. Matter 2011 with permission of the copyright owner[65]. **(b)** Adaptive X-ray focusing using deformable mirrors. (i), (ii) Photographs of a deformable mirror and an assembled mirror. (iii*)* Measured beam profile. The figure was modified from Goto et al., Rev. Sci. Instrum. 2015 with permission of the copyright owner[66].

Fig 18. (a) Live bacterial imaging with an X-ray focusing system at SACLA, an X-ray free-electron laser (XFEL) facility, by Kimura et al[42]. Pulsed coherent X-ray solution scattering (PCXSS) using X-ray laser diffraction was applied to live bacteria. **(i)** A micro-liquid enclosure array (MLEA) can retain biological samples in solution between two silicon nitride membranes. (ii, iii) A live-dead experiment indicated that 99% of the *Microbacterium lacticum* cells were alive in MLEA at 1 h after enclosure in the XFEL. (ii) Soon after exposure, (iii) At 1 h after enclosure. (iv) A scanning electron microscopy (SEM) image of the bacteria. Scale bar: 500 nm. (v) Reconstructed image of an *M. lacticum* cell by PCXSS. Scale bar: 100 nm. (vi) TEM image of an *M. lacticum* cell. Scale bar: 100 nm. The figures were modified from Kimura et al, 2014 with permission of the copyright owner[42]. **(b)** Scanning CXDI, so-called X-ray ptychography, with high-resolution using focused X-ray beams by Takahashi et al. (i) SEM image of magnetotactic bacteria MO-1. (ii) Phase map of MO-1 obtained by dark-field X-ray ptychography. (iii) Magnification of the lower-right bacterium in (ii). The figures were modified from Takahashi et al., PNAS 2014 with permission of the copyright owner[69].

References

1. P. Goby, *Une application nouvelle des rayons X: la microradiographie*, 1913.
2. P. Kirkpatrick and A. V. Baez, *JOSA*, 1948, **38**, 766-774.
3. H. Wolter, *Annalen der Physik*, 1952, **445**, 94-114.
4. B. Niemann, D. Rudolph and G. Schmahl, *Optics Communications*, 1974, **12**, 160-163.
5. B. Niemann, D. Rudolph and G. Schmahl, *Applied Optics*, 1976, **15**, 1883-1884.
6. G. Schmahl, *Optik*, 1969, **29**, 577-585.
7. C. Jacobsen, J. Kirz, williams and S. Williams, *Ultramicroscopy*, 1992, **47**, 55-79.
8. G. Schmahl, Chenogolovka, Russia, 1993.
9. M. Moronne, C. Larabell, P. R. Selvin and A. I. von Brenndorff, 1994.
10. W. Yun, P. Viccaro, B. Lai and J. Chrzas, *Review of scientific instruments*, 1992, **63**, 582-585.
11. B. Lai, W. Yun, D. Legnini, Y. Xiao, J. Chrzas, P. Viccaro, V. White, S. Bajikar, D. Denton and F. Cerrina, *Applied physics letters*, 1992, **61**, 1877-1879.
12. A. Krasnoperova, J. Xiao, F. Cerrina, E. Di Fabrizio, L. Luciani, M. Figliomeni, M. Gentili, W. Yun, B. Lai and E. Gluskin, *Journal of Vacuum Science & Technology B: Microelectronics and Nanometer Structures Processing, Measurement, and Phenomena*, 1993, **11**, 2588-2591.
13. D. Bilderback, S. Hoffman and D. Thiel, *Science*, 1994, **263**, 201-203.
14. D. Bilderback, D. Thiel, R. Pahl and K. Brister, *Journal of synchrotron radiation*, 1994, **1**, 37-42.
15. C. Buckley, G. Foster, R. Burge, S. Ali, C. Scotchford, J. Kirz and M. Rivers, *Review of scientific instruments*, 1992, **63**, 588-590.
16. I. Nakai, Y. Terada, M. Itou and Y. Sakurai, *Journal of synchrotron radiation*, 2001, **8**, 1078-1081.
17. J. Kawai, K. Takagawa, S. Fujisawa, A. Ektessabi and S. Hayakawa, *Journal of trace and microprobe techniques*, 2001, **19**, 541-546.
18. P. Kirkpatrick and A. V. Baez, *J Opt Soc Am*, 1948, **38**, 766-774.
19. K. Yamauchi, H. Mimura, K. Inagaki and Y. Mori, *Rev Sci Instrum*, 2002, **73**, 4028-4033.
20. S. Matsuyama, H. Mimura, H. Yumoto, H. Hara, K. Yamamura, Y. Sano, K. Endo, Y. Mori, M. Yabashi, Y. Nishino, K. Tamasaku, T. Ishikawa and K. Yamauchi, *Rev Sci Instrum*, 2006, **77**.
21. I. Snigireva and A. Snigirev, *Journal of Environmental Monitoring*, 2006, **8**, 33-42.
22. B. Crone, M. Aschner, T. Schwerdtle, U. Karst and J. Bornhorst, *Metallomics*, 2015, **7**, 1189-1195.
23. R. M. Godinho, M. T. Cabrita, L. C. Alves and T. Pinheiro, *Metallomics*, 2014, **6**, 1626-1631.
24. C. M. Thompson, J. Seiter, M. A. Chappell, R. V. Tappero, D. M. Proctor, M. Suh, J. C. Wolf, L. C. Haws, R. Vitale, L. Mittal, C. R. Kirman, S. M. Hays and

M. A. Harris, *Toxicol Sci*, 2015, **143**, 16-25.
25. M. Shimura, A. Saito, S. Matsuyama, T. Sakuma, Y. Terui, K. Ueno, H. Yumoto, K. Yamauchi, K. Yamamura, H. Mimura, Y. Sano, M. Yabashi, K. Tamasaku, K. Nishio, Y. Nishino, K. Endo, K. Hatake, Y. Mori, Y. Ishizaka and T. Ishikawa, *Cancer Res*, 2005, **65**, 4998-5002.
26. L. Szyrwiel, M. Shimura, J. Shirataki, S. Matsuyama, A. Matsunaga, B. Setner, L. Szczukowski, Z. Szewczuk, K. Yamauchi, W. Malinka, L. Chavatte and R. Lobinski, *Metallomics*, 2015, **7**, 1155-1162.
27. G. S. Montanha, E. S. Rodrigues, J. P. R. Marques, E. de Almeida, A. R. dos Reis and H. W. P. de Carvalho, *Metallomics*, 2020.
28. E. S. Rodrigues, M. H. Gomes, N. M. Duran, J. G. Cassanji, T. N. da Cruz, A. Sant'Anna Neto, S. M. Savassa, E. de Almeida and H. W. Carvalho, *Frontiers in plant science*, 2018, **9**, 1588.
29. R. Ortega, G. Deves and A. Carmona, *Journal of the Royal Society Interface*, 2009, **6**, S649-S658.
30. S. Matsuyama, H. Mimura, H. Yumoto, Y. Sano, K. Yamamura, M. Yabashi, Y. Nishino, K. Tamasaku, T. Ishikawa and K. Yamauchi, *Rev Sci Instrum*, 2006, **77**, 103102.
31. S. Matsuyama, H. Mimura, K. Katagishi, H. Yumoto, S. Handa, M. Fujii, Y. Sano, M. Shimura, M. Yabashi, Y. Nishino, K. Tamasaku, T. Ishikawa and K. Yamauchi, *Surf Interface Anal*, 2008, **40**, 1042-1045.
32. S. Matsuyama, M. Shimura, H. Mirnura, M. Fujii, H. Yumoto, Y. Sano, M. Yabashi, Y. Nishino, K. Tamasaku, T. Ishikawa and K. Yamauchi, *X-Ray Spectrom*, 2009, **38**, 89-94.
33. P. Walther, D. Studer and K. McDonald, *Microscopy and Microanalysis*, 2007, **13**, 440-441.
34. P. Bennett, G. Foster, C. Buckley and R. Burge, *Journal of microscopy*, 1993, **172**, 109-119.
35. J. Kirz, C. Jacobsen and M. Howells, *Quarterly reviews of biophysics*, 1995, **28**, 33-130.
36. K. Sakai and S. Okada, *Radiation research*, 1984, **98**, 479-490.
37. A. D. Stead, R. A. Cotton, A. M. Page, M. D. Dooley and T. W. Ford, 1993.
38. S. Williams, X. Zhang, C. Jacobsen, J. Kirz, S. Lindaas, J. Van't Hof and S. Lamm, *Journal of Microscopy*, 1993, **170**, 155-165.
39. S. Matsuyama, M. Shimura, M. Fujii, K. Maeshima, H. Yumoto, H. Mimura, Y. Sano, M. Yabashi, Y. Nishino, K. Tamasaku, Y. Ishizaka, T. Ishikawa and K. Yamauchi, *X-Ray Spectrom*, 2010, **39**, 260-266.
40. M. Debeljak, J. T. van Elteren and K. Vogel-Mikus, *Anal Chim Acta*, 2013, **787**, 155-162.
41. S. Matsuyama, A. Matsunaga, S. Sakamoto, Y. Iida, Y. Suzuki, Y. Ishizaka, K. Yamauchi, T. Ishikawa and M. Shimura, *Metallomics*, 2013, **5**, 492-500.
42. T. Kimura, Y. Joti, A. Shibuya, C. Song, S. Kim, K. Tono, M. Yabashi, M. Tamakoshi, T. Moriya and T. Oshima, *Nature communications*, 2014, **5**, 3052.
43. S. Matsuyama, J. Yamada, Y. Kohmura, M. Yabashi, T. Ishikawa and K. Yamauchi, *Optics express*, 2019, **27**, 18318-18328.
44. J. E. Heuser, T. Reese and D. M. Landis, *Cold Spring Harbor Symposia on Quantitative Biology*, 1976, **40**, 17-24.

45. S. Chen, J. Deng, Y. Yuan, C. Flachenecker, R. Mak, B. Hornberger, Q. Jin, D. Shu, B. Lai and J. Maser, *Journal of synchrotron radiation*, 2013, **21**, 66-75.
46. K. Tokuyasu, *Journal of ultrastructure research*, 1978, **63**, 287-307.
47. G. Griffiths, J.-W. Slot and P. Webster, *Journal*, 2015.
48. M. Shimura, H. Shindou, L. Szyrwiel, S. M. Tokuoka, F. Hamano, S. Matsuyama, M. Okamoto, A. Matsunaga, Y. Kita and Y. Ishizaka, *The FASEB Journal*, 2016, **30**, 4149-4158.
49. M. Endrizzi, *Nuclear instruments and methods in physics research section A: Accelerators, spectrometers, detectors and associated equipment*, 2018, **878**, 88-98.
50. A. Momose, *Japanese journal of applied physics*, 2005, **44**, 6355.
51. K. A. Nugent, *Advances in Physics*, 2010, **59**, 1-99.
52. J. Miao, P. Charalambous, J. Kirz and D. Sayre, *Nature*, 1999, **400**, 342-344.
53. D. Sayre, *Acta Crystallographica*, 1952, **5**, 843-843.
54. J. R. Fienup, *Optics letters*, 1978, **3**, 27-29.
55. Y. Nishino, Y. Takahashi, N. Imamoto, T. Ishikawa and K. Maeshima, *Physical review letters*, 2009, **102**, 018101.
56. K. Maeshima, R. Imai, S. Tamura and T. Nozaki, *Chromosoma*, 2014, **123**, 225-237.
57. Y. Nishino, M. Eltsov, Y. Joti, K. Ito, H. Takata, Y. Takahashi, S. Hihara, A. S. Frangakis, N. Imamoto and T. Ishikawa, *The EMBO journal*, 2012, **31**, 1644-1653.
58. Y. Joti, T. Hikima, Y. Nishino, F. Kamada, S. Hihara, H. Takata, T. Ishikawa and K. Maeshima, *Nucleus*, 2012, **3**, 404-410.
59. K. Maeshima, R. Rogge, S. Tamura, Y. Joti, T. Hikima, H. Szerlong, C. Krause, J. Herman, E. Seidel and J. DeLuca, *The EMBO journal*, 2016, **35**, 1115-1132.
60. C. He, L. G. Fong, S. G. Young and H. Jiang, *Journal of Investigative Medicine*, 2017, **65**, 669-672.
61. E. Carboni, J.-D. Nicolas, M. Töpperwien, C. Stadelmann-Nessler, P. Lingor and T. Salditt, *Biomedical optics express*, 2017, **8**, 4331-4347.
62. M. Eriksson, J. F. van der Veen and C. Quitmann, *Journal of synchrotron radiation*, 2014, **21**, 837-842.
63. M. Yabashi, K. Tono, H. Mimura, S. Matsuyama, K. Yamauchi, T. Tanaka, H. Tanaka, K. Tamasaku, H. Ohashi and S. Goto, *Journal of synchrotron radiation*, 2014, **21**, 0-0.
64. H. Mimura, S. Handa, T. Kimura, H. Yumoto, D. Yamakawa, H. Yokoyama, S. Matsuyama, K. Inagaki, K. Yamamura and Y. Sano, *Nature Physics*, 2010, **6**, 122-125.
65. K. Yamauchi, H. Mimura, T. Kimura, H. Yumoto, S. Handa, S. Matsuyama, K. Arima, Y. Sano, K. Yamamura and K. Inagaki, *Journal of Physics: Condensed Matter*, 2011, **23**, 394206.
66. T. Goto, H. Nakamori, T. Kimura, Y. Sano, Y. Kohmura, K. Tamasaku, M. Yabashi, T. Ishikawa, K. Yamauchi and S. Matsuyama, *Rev Sci Instrum*, 2015, **86**, 043102.
67. M. M. Seibert, T. Ekeberg, F. R. Maia, M. Svenda, J. Andreasson, O. Jönsson, D. Odić, B. Iwan, A. Rocker and D. Westphal, *Nature*, 2011, **470**, 78-81.
68. Y. Nishino, T. Kimura, A. Suzuki, Y. Joti and Y. Bessho, Coherent Imaging Using SACLA, https://www.jstage.jst.go.jp/article/jcrsj/59/1/59_18/_pdf).

69. A. Suzuki, K. Shimomura, M. Hirose, N. Burdet and Y. Takahashi, *Scientific reports*, 2016, **6**, 35060.

Fig 1

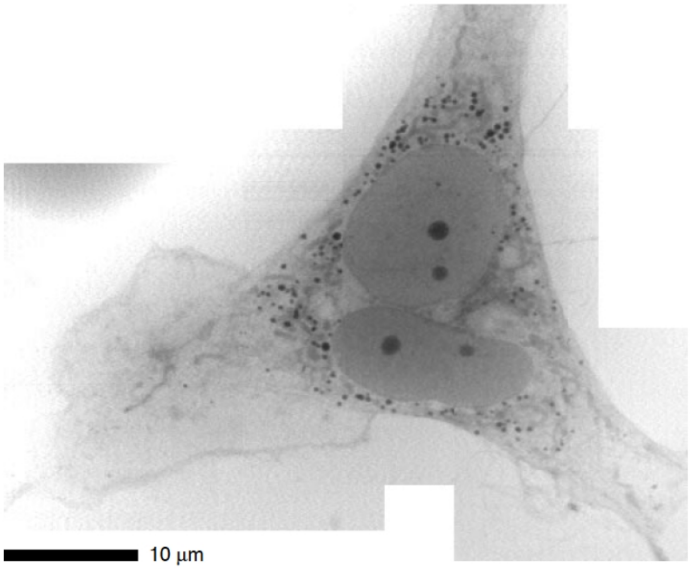

Fig 1. Scanning X-ray transmission micrograph (STXM) of fibroblasts by Gilbert in the 1990s[35]. Reproduced with permission of the copyright owner.

Fig 2

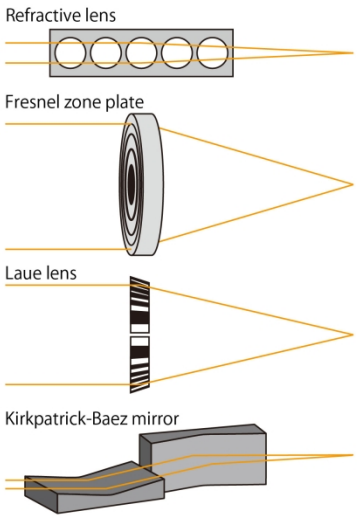

Fig 2. Representative X-ray focusing systems.

Fig 3

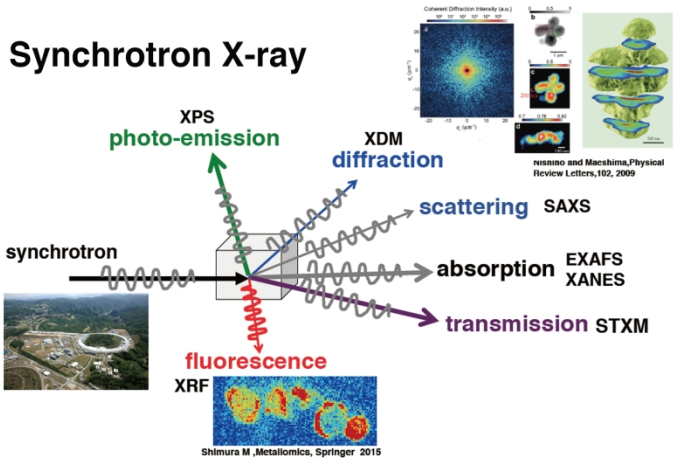

Fig 3. Many ways to use synchrotron X-rays.

Fig 4

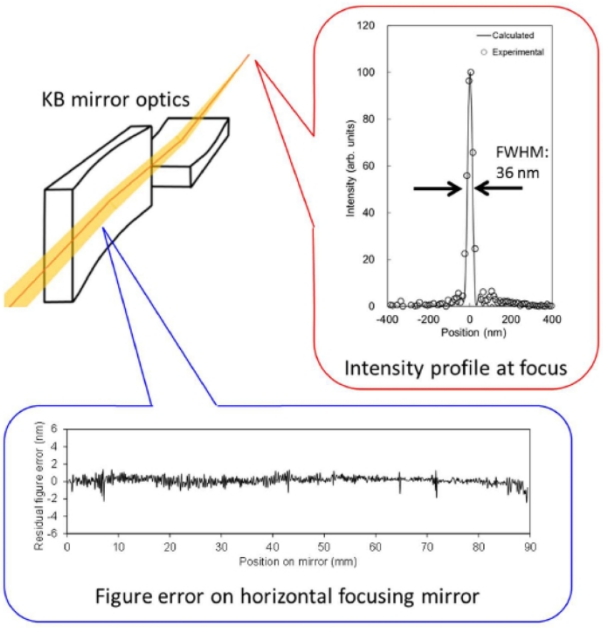

Fig 4. Schematic of Kirkpatrick-Baez (KB) mirror optics together with the residual error in the elliptical shape and characterized intensity profile at the focus in the vertical direction.

Fig 5

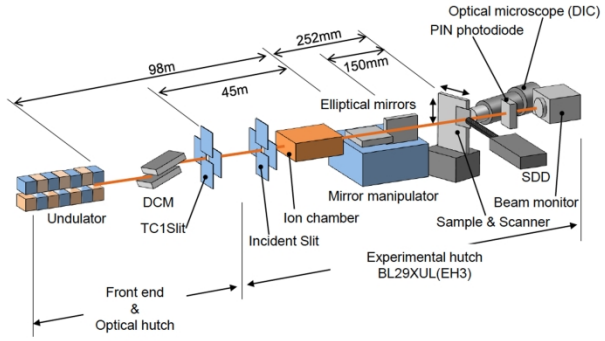

Fig 5. Schematic of the scanning X-ray fluorescence microscopy (SXFM) system.

Fig 6

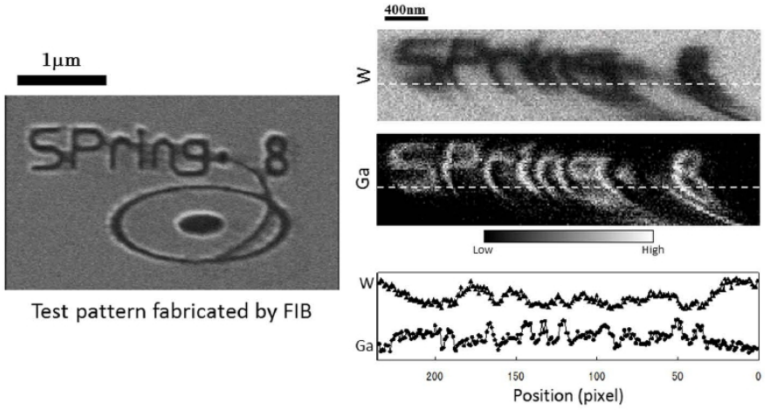

Fig 6. High-resolution W and Ga maps of a test pattern. Left, Ga test pattern prepared by focused ion beam (FIB). Right, SXFM images of the W and Ga test pattern. Exposure = 1 s/pixel, scanning step = 15 nm/pixel, and X-ray energy = 15 keV. The figure was reproduced from Matsuyama et al., Rev. Sci. Instrum. 2006 with permission of the copyright owner[30].

Fig 7

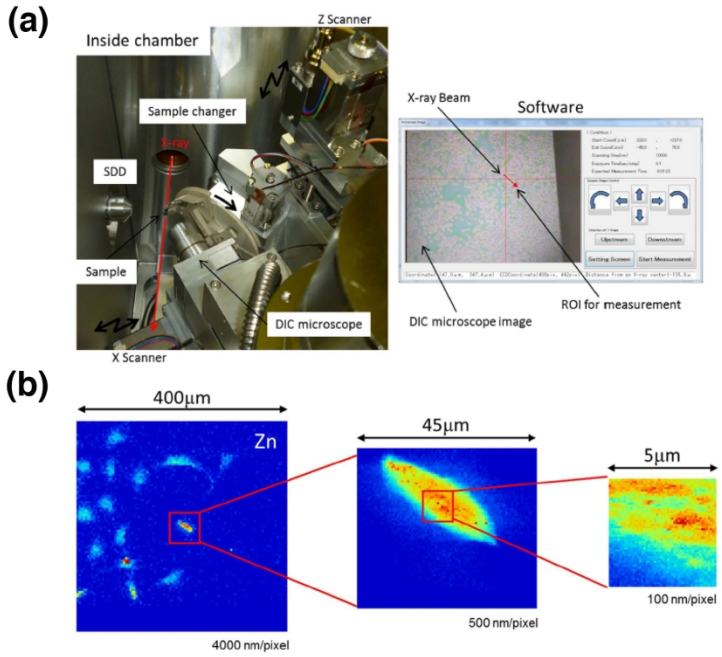

Fig 7. SXFM became user friendly. (a), Photograph of the user-friendly SXFM (left) and graphical user interface-based software (right). (b), Zoom function of the SXFM. The sample was HeLa cells. X-ray energy = 15 keV.

Fig 8

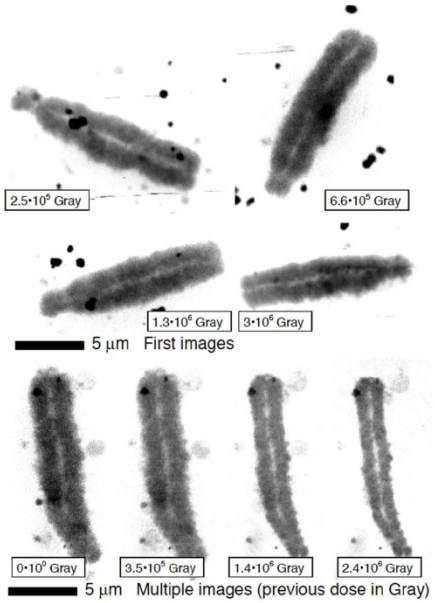

Fig 8. Radiation damage to wet chromosomes reported by Williams in the 1990s[38]. V. faba chromosomes were fixed with 0.2% glutaraldehyde and imaged by scanning transmission X-ray microscopy (STXM) in physiological buffer. Multiple images of the same chromosome showed degradation due to radiation damage (lower); however, the initial images (First images) showed mass and diameter measurements similar to those of the previously unexposed ones (0-10^0 Gy, Multiple images). Reproduced with permission of the copyright owner.

Fig 9

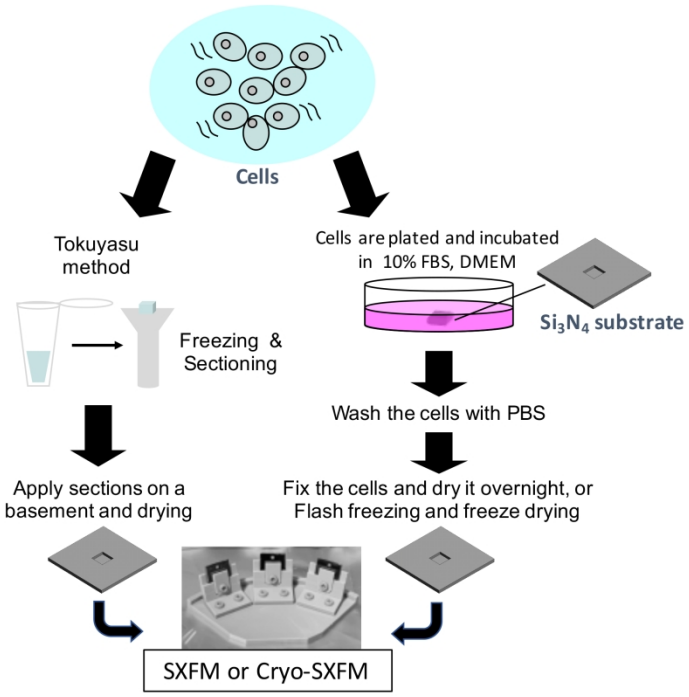

Fig 9. Diagram showing sample preparation protocols for SXFM. The inset photo shows a sample holder that can set three samples on a motorized stage for SXFM (see Section 2.3 User-friendly upgrades to SXFM).

Fig 10

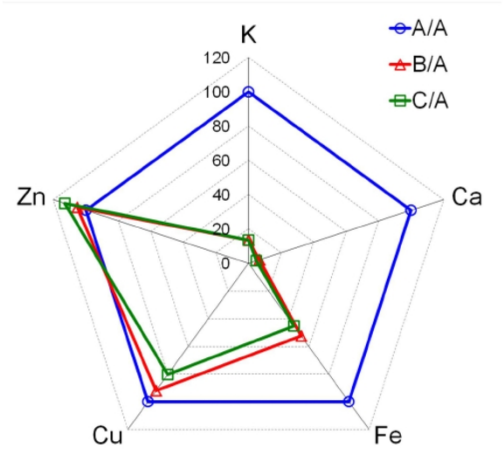

Fig 10. Leakage of intracellular elements due to fixation. Average elemental contents (K, Ca, Fe, Cu, and Zn) of cells measured by inductively coupled plasma-mass spectrometry (ICP-MS). Sample preparation is described below. A, Cells were cultured for 2 days and then 10^7 cells were collected by centrifugation. B, Cells were washed with PBS and fixed with 4% paraformaldehyde in PBS for 10 min. C, Cells were permeabilized for 5 min with 0.2% Triton X-100 (Sigma-Aldrich, St. Louis, MO) in PBS, washed with PBS. The K, Ca, Fe, Cu, and Zn contents of samples A, B, and C were measured by ICP-MS. The axis in the chart shows the ratios of B and C to A. The figure was reproduced from Matsuyama et al., X-ray Spectrom., X-ray Spectrom. 2010 with permission of the copyright owner[39].

Fig 11

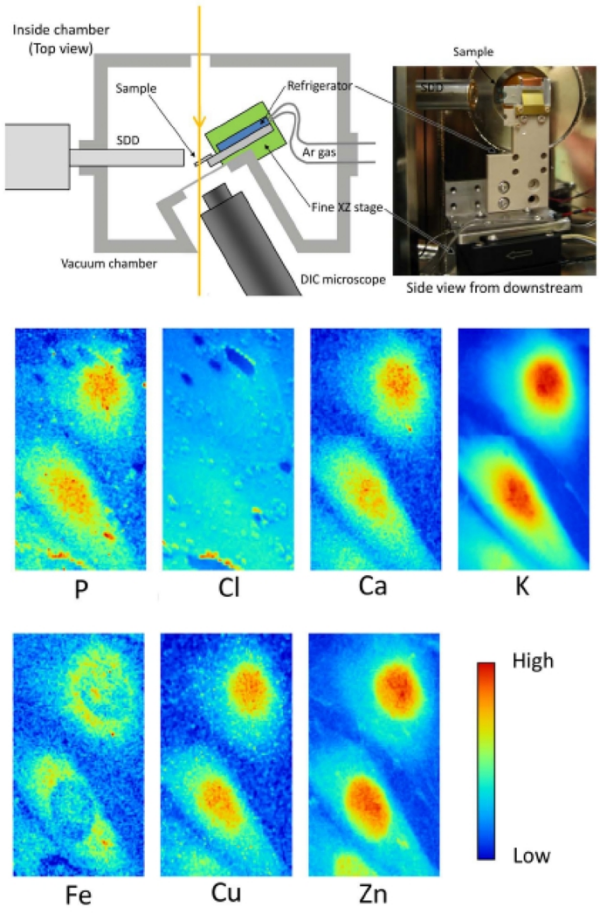

Fig 11. Schematic and photograph of cryo-scanning x-ray fluorescence microscopy (SXFM) (top), and elemental distribution maps of frozen-hydrated cells (bottom). The figure was reproduced from Matsuyama et al., X-ray Spectrom. 2010 with permission of the copyright owner[39].

Fig 12

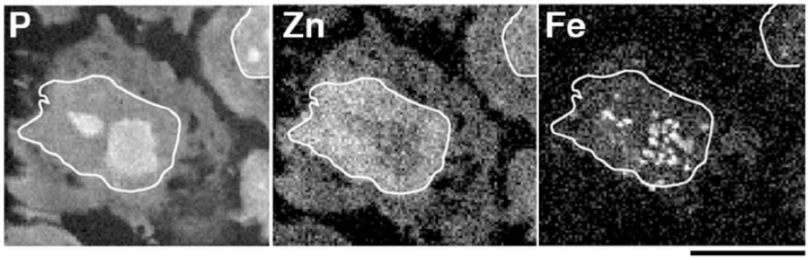

Fig 12. Images of intracellular P, Zn, and Fe mapping in multiple myeloma cells. Photographs of cryo-sections (500 nm thick) of cells were obtained using the following parameters: exposure = 1 s/pixel, scanning step = 250 nm/pixel, X-ray energy = 15 keV. Bar, 10 μm. The white border indicates the nuclear region. The figure was reproduced from Shimura and Matsuyama, JSR 2010 with permission of the copyright owner.

Fig 13

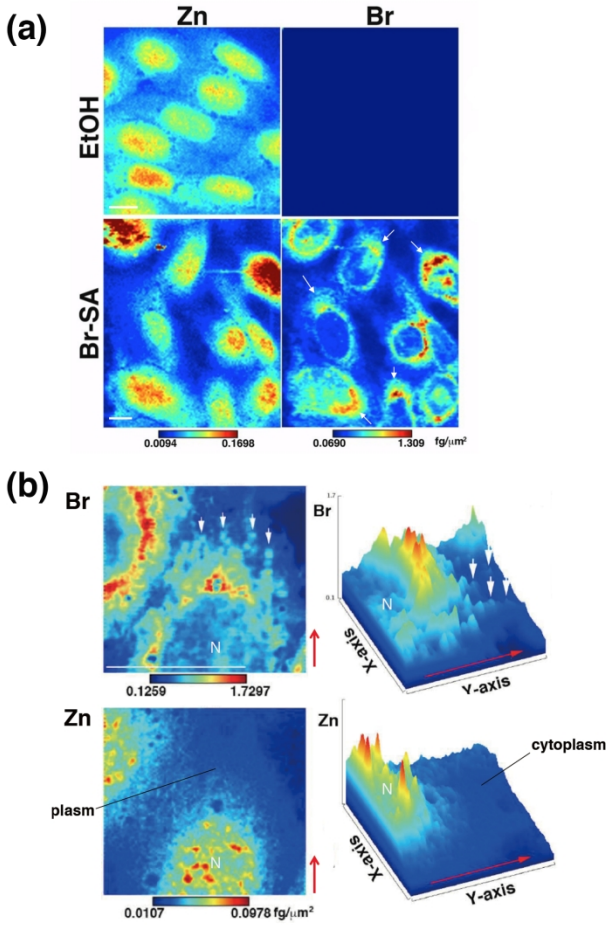

Fig 13. SXFM images of Br-labeled fatty acid. (a) Zn-, and Br-mapping images of Br-labeled stearic acids (Br-SA) and EtOH-treated CHO-K1 cells. Cells were treated with Br-SA for 24 h. Br and Zn mapping images taken with 600 nm/pixel X-ray beam size. Arrows indicate the Br signals, which tended to be clustered. (b) Higher-resolution X-ray fluorescence images of Br-labeled palmitic acid (Br-PA). Left, Br and Zn mapping images taken with an X-ray beam size of 250 nm/pixel. Cells were treated with Br-PA for 24 h. Right, a surface plot generated based on the red area in the left images. Red arrows, the direction presented in the surface plots; white arrows, the spot-like Br distribution. Br, BrKα X-ray emission line. A brighter color indicates higher signal intensity. Color bar, fg/μm^2; bar, 10 μm. The figures were modified from Shimura, FASEB J 2016 with permission of the copyright owner[48].

Fig 14

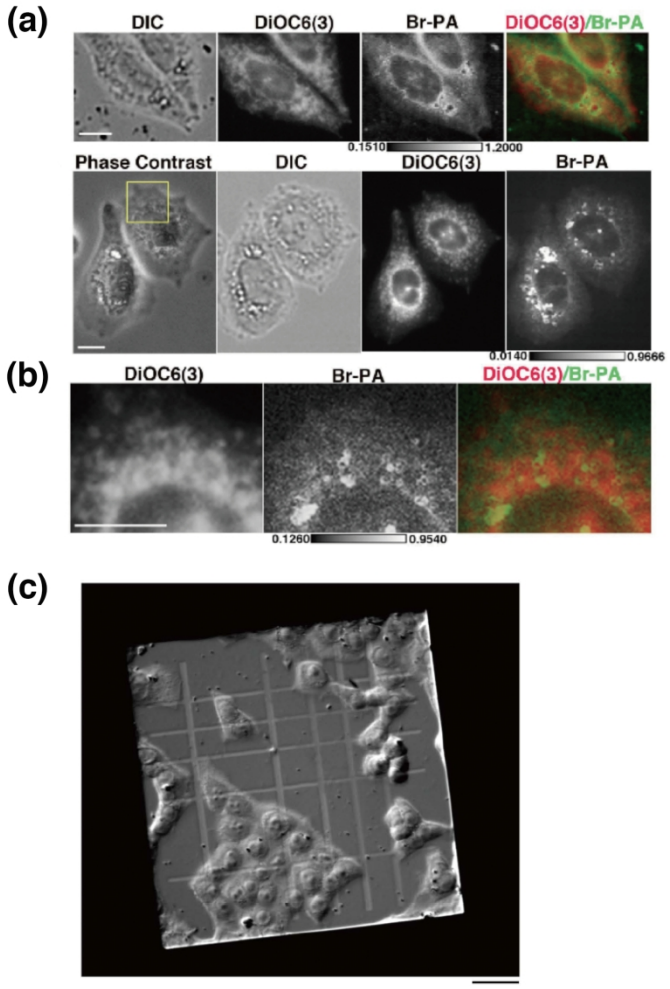

Fig 14. Merged images from different microscopies. (a) Comparison between a marker of endoplasmic reticulum, DiOC6(3) fluorescence image and Br signals from SXFM (500 nm/pixel). (b) The area framed in yellow in (a) was observed using higher-resolution SXFM (250 nm/pixel). DIC, differential interference contrast images; DiOC6(3), fluorescence dye signals; Br-PA, SXFM signals from BrKα; phase-contrast, phase-contrast images. Merged image, red, DiOC6(3); green, Br; bar, 10 μm; bar in Br, fg/μm^2. (c) DIC images of a 200-nm-thick gridded SiN basement. Cells were plated on the basement, fixed with paraformaldehyde and dried overnight at room temperature. DIC, differential interference contrast microscopy; Bar, 20 μm. The figures were modified from Shimura, FASEB J 2016[48].

Fig 15

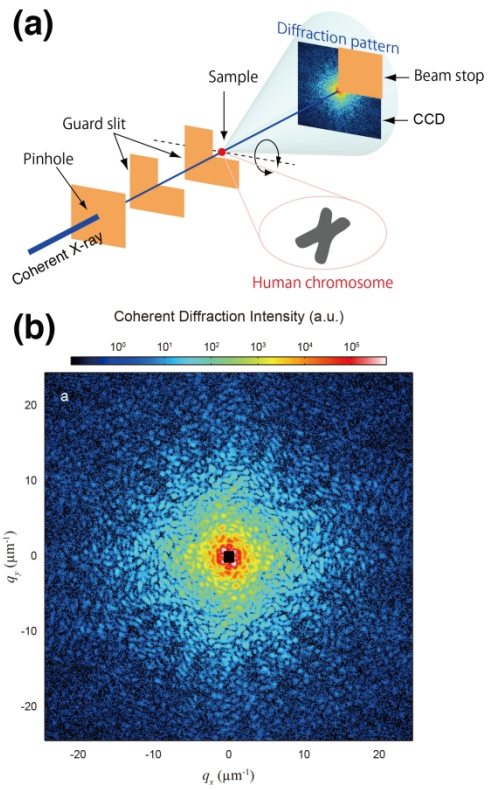

Fig 15. X-ray diffraction microscopy (XDM) for observation of chromosomes in cells. (a) Schematic view of XDM measurement of an unstained human chromosome at BL29XUL in SPring-8. (b) The coherent diffraction (speckles) from the chromosome. The panels were reproduced from Nishino et al., 2009[55] with permission of the copyright owner.

Fig 16

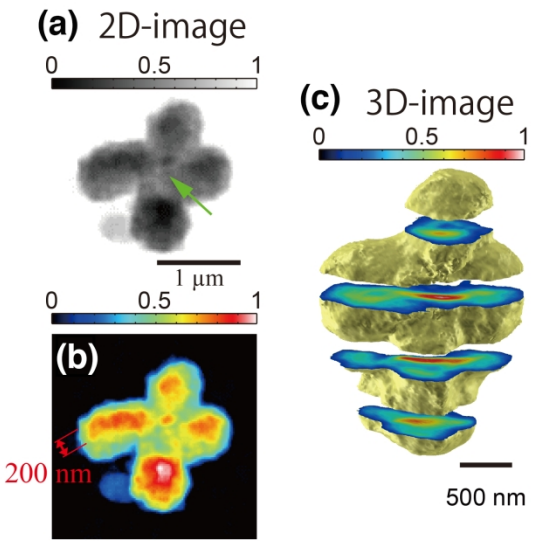

Fig 16. A two-dimensional reconstruction of a human chromosome is shown in grayscale, (a) and color, (b). Note that the intensities are proportional to the projection of the electron density. An arrow indicates the centromere region. (c), Reconstructed 3D electron-density map of the chromosome. Cross-sectional images of the chromosome at 409-nm intervals are shown. The panels were reproduced from Nishino et al., 2009[55] with permission of the copyright owner.

Fig 17

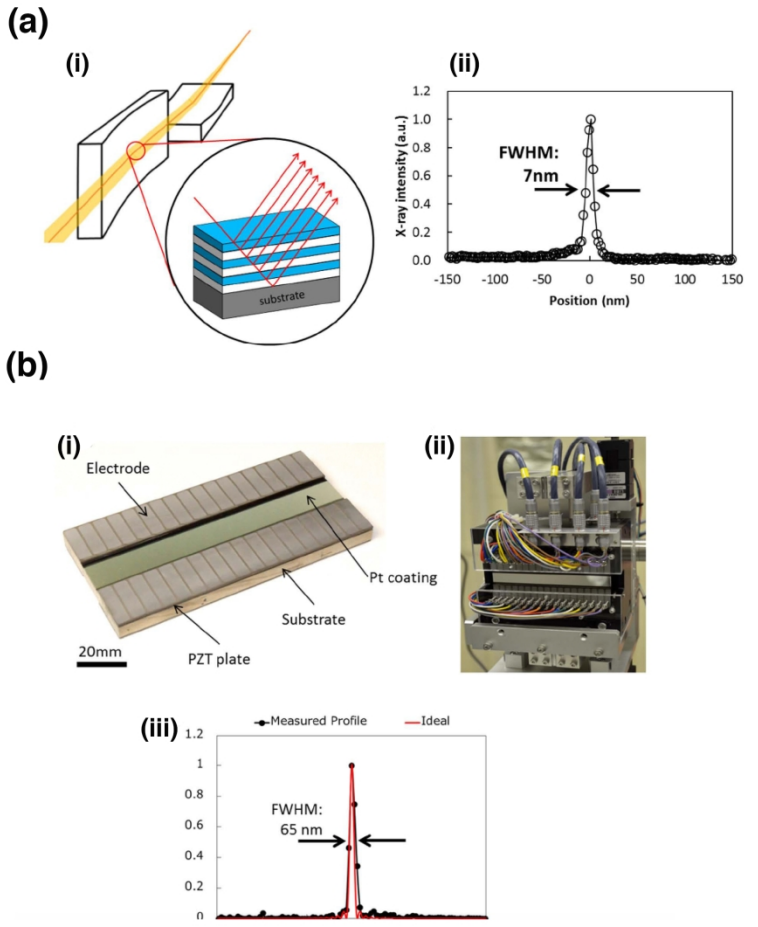

Fig 17. Future SXFM technologies. (a) X-ray focusing using multilayer KB mirrors. (i) Schematic and (ii) obtained beam profile at the focus. The figure was reproduced from Yamauchi et al., J. Phys. Condens. Matter 2011 with permission of the copyright owner[65]. (b) Adaptive X-ray focusing using deformable mirrors. (i), (ii) Photographs of a deformable mirror and an assembled mirror. (iii) Measured beam profile. The figure was modified from Goto et al., Rev. Sci. Instrum. 2015 with permission of the copyright owner[66].

Fig 18

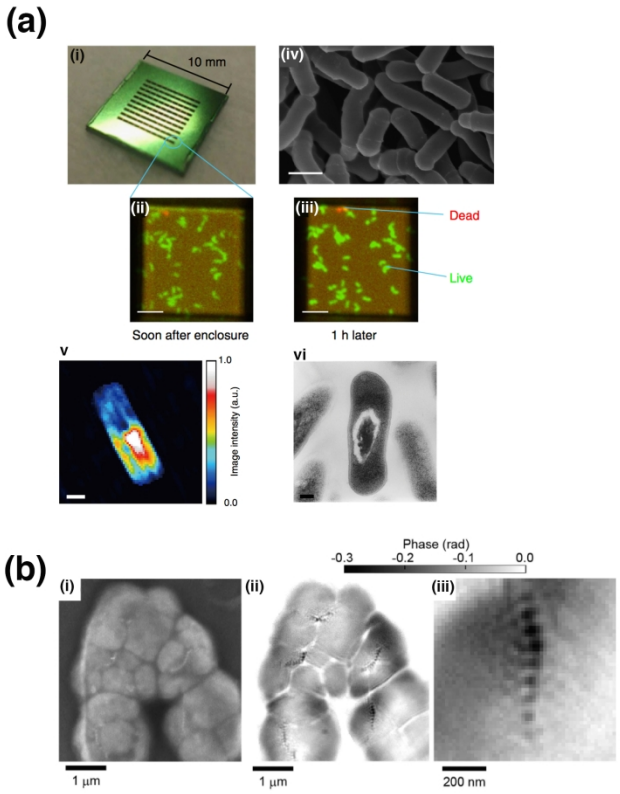

Fig 18. (a) Live bacterial imaging with an X-ray focusing system at SACLA, an X-ray free-electron laser (XFEL) facility, by Kimura et al[42]. Pulsed coherent X-ray solution scattering (PCXSS) using X-ray laser diffraction was applied to live bacteria. (i) A micro-liquid enclosure array (MLEA) can retain biological samples in solution between two silicon nitride membranes. (ii, iii) A live-dead experiment indicated that 99% of the Microbacterium lacticum cells were alive in MLEA at 1 h after enclosure in the XFEL. (ii) Soon after exposure, (iii) At 1 h after enclosure. (iv) A scanning electron microscopy (SEM) image of the bacteria. Scale bar: 500 nm. (v) Reconstructed image of an M. lacticum cell by PCXSS. Scale bar: 100 nm. (vi) TEM image of an M. lacticum cell. Scale bar: 100 nm. The figures were modified from Kimura et al, 2014 with permission of the copyright owne[r42]. (b) Scanning CXDI, so-called X-ray ptychography, with high-resolution using focused X-ray beams by Takahashi et al. (i) SEM image of magnetotactic bacteria MO-1. (ii) Phase map of MO-1 obtained by dark-field X-ray ptychography. (iii) Magnification of the lower-right bacterium in (ii). The figures were modified from Takahashi et al., PNAS 2014 with permission of the copyright owner[69].